Available online at www.sciencedirect.com

ScienceDirect

Procedia Manufacturing 48 (2020) 873–881

Procedia MANUFACTURING

www.elsevier.com/locate/procedia

48th SME North American Manufacturing Research Conference, NAMRC 48 (Cancelled due to COVID-19)

Digital force prediction for milling

Michael Gomez[a,b], Timothy No[a], and Tony Schmitz[a,b]*

[a]*University of Tennessee, Knoxville, 1512 Middle Dr., Knoxville, TN 37996, USA*
[b]*Oak Ridge National Laboratory, Manufacturing Demonstration Facility, 2370 Cherahala Blvd., Knoxville, TN 37932, USA*

* Corresponding author. Tel.: +1-865-974-6141. *E-mail address:* tony.schmitz@utk.edu

Abstract

This paper presents a fully digital, integrated approach for milling force prediction with arbitrary end mill-work material combinations. The approach includes: 1) structured light scanning to identify the end mill's cutting edge macro-geometry along the tool axis; 2) structured light scanning to measure the cutting edge cross-sectional rake and relief profiles; 3) finite element analysis of orthogonal cutting to determine the force model coefficients that relate the force to chip area using the work material's constitutive model and tool's rake and relief profiles; and 4) time domain simulation with inputs that include the measured cutting edge macro-geometry, finite element-based force model, and measured structural dynamics. Milling force predictions are compared to in-process measurements to validate the method.

Keywords: Machining; force; modeling; structured light; finite element analysis; digital twin

1. Introduction*

Digital modeling is ubiquitous in part production by machining. What was once a two-dimensional landscape dominated by paper-based engineering drawings is now a three-dimensional computer-aided design (CAD)/computer-aided manufacturing (CAM) infrastructure. In this relatively new paradigm, component solid models are used to generate computer numerically controlled (CNC) part programs. These M and G code instructions prescribe the required relative motions between the initial material stock, which may be a block, forging, casting, or additively manufactured preform, and the rotating end mill used to remove material and obtain the desired geometry and surface finish.

Digital modeling is also applied to aid in selection of operating parameters that result in a process that repeatably produces in-tolerance parts at maximum profit. For milling, this modeling includes the process dynamics, which encompasses both stability (i.e., stable operation, which exhibits only forced vibration, versus unstable performance that demonstrates self-excited vibration or period-n bifurcations and the corresponding degradation in part quality) and surface location error, or part geometry errors that occur due to the phasing between the tool-part relative motions and the instant the final surface is generated [1-3]. In both cases, the required modeling inputs are: 1) the tool geometry; 2) the force model that relates the cutting force required to shear away the material to the commanded chip area; and 3) the structural dynamics of the tool-holder-spindle-machine-workpiece combination.

In this paper, a digital modeling approach that includes: structured light scanning to identify the end mill's cutting edge macro-geometry along the tool axis; structured light scanning

*Notice: This manuscript has been authored by UT-Battelle, LLC, under contract DE-AC05-00OR22725 with the US Department of Energy (DOE). The US government retains and the publisher, by accepting the article for publication, acknowledges that the US government retains a nonexclusive, paid-up, irrevocable, worldwide license to publish or reproduce the published form of this manuscript, or allow others to do so, for US government purposes. DOE will provide public access to these results of federally sponsored research in accordance with the DOE Public Access Plan (http://energy.gov/downloads/doe-public-access-plan).

10.1016/j.promfg.2020.05.125

to measure the rake and relief profiles; finite element analysis of orthogonal cutting to determine the force model coefficients using the work material's constitutive model and tool's rake and relief edge geometries; and time domain simulation with inputs that include the cutting edge macro-geometry, force model, and structural dynamics. The outcome is the ability to predict milling force for any end mill-work material combination in a fully digital, integrated approach.

Nomenclature

r	radius of point on end mill cutting edge
ϕ	angle of point on end mill cutting edge
z	position along end mill axis
$\Delta\phi$	angular resolution in time domain simulation
SR	steps per revolution in time domain simulation
RO	runout for point on end mill cutting edge
F_t	tangential component of cutting force
F_n	normal component of cutting force
k_t	cutting force coefficient for tangential component
k_n	cutting force coefficient for normal component
m	modal mass
c	modal viscous damping coefficient
k	modal stiffness
x	feed direction for end milling operation
y	perpendicular direction to x in the cut plane
F_x	x component of cutting force
F_y	y component of cutting force

2. Background

Modeling of machining operations has received continuous international attention since the mid-20th century [1-3]. A subset of these efforts has included a specific focus on modeling the performance based on the end mill geometry. For example, multiple authors have modeled the performance of inserted cutters. Fu *et al.* predicted the forces in face milling for various cutting conditions and cutter geometries [4]. Kim and Ehmann simulated the static and dynamic cutting forces in face milling [5]. Zheng *et al.* modeled face milling as the simultaneous action of multiple single point cutting tools [6]. Engin and Altintas presented a generalized inserted cutter model for predicting cutting force, vibration, surface finish, and stability in milling, where the cutting edge locations were defined mathematically [7-8].

Authors have also examined non-standard cutting edge geometries. Wang and Yang [9] presented force models in the angle and frequency domains for a cylindrical roughing end mill with sinusoidal cutting edges. Merdol and Altintas [10] modeled the serration profile by fitting points along a cubic spline projected on the helical flutes. This geometric model was used to generate a time domain milling model. Dombovari *et al.* [11] used the semi-discretization method to analyze the stability of serrated end mills. Later, he and others created general models for various tool geometries [12-13]. Koca and Budak [14] used a linear edge-force model and the semi-discretization method for force and stability modeling and optimized the serration waveform shape to reduce milling forces and increase stability. Grabowski *et al.* [15] extended their mechanistic model to calculate the process forces of serrated endmills. Tehranizadeh and Budak [16] proposed a genetic algorithm to optimize the design of serration shapes. No *et al.* performed force and stability modeling for non-standard geometry end mills [17-18].

Typically, the design details of non-standard geometry endmills is not available. Through a reverse engineering strategy, the three-dimensional surface of the endmill is reconstructed and used for simulation purposes [17-18]. This paper builds on prior efforts by implementing scanning metrology to measure the cutting edge macro-geometry and cross-sectional profile, applying finite element analysis to determine the force model by direct use of the measured edge rake and relief angle geometry, and including both within a time domain simulation to enable fully digital force prediction.

3. Scanning metrology for edge geometry

Structured light scanning metrology was used to collect a point cloud from the complex end mill surfaces and develop the corresponding solid model. In this technique, a pattern of parallel lines is projected onto the end mill surface and the reflected lines are distorted due to the surface geometry. The measurement system then uses the relative positions of the projector and two cameras together with the distorted lines to reconstruct the three-dimensional surface. While many commercial options are available, the GOM ATOS Capsule system was used for this research. The measurements proceeded by first preparing the end mill surface using a removable anti-glare coating and attaching reference targets to the tool's shank surface to enable multiple measurements to be stitched together and generate the solid model. Second, multiple scans (23 total) were completed to obtain the point cloud and 3D digital model [17-18]; see Appendix A.

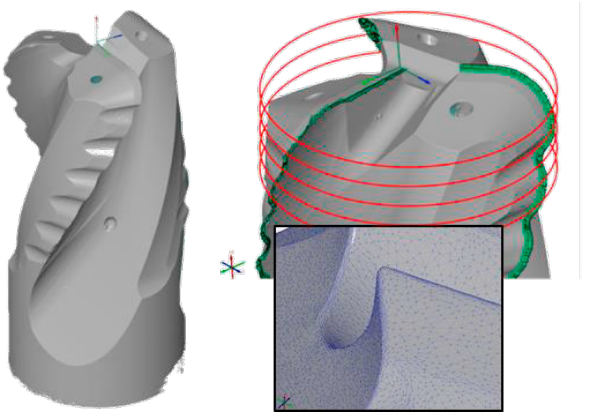

Fig. 1. (Left) 3D model from structured light scan for end mill (Walter Tools, part number 3D1163-6768616). (Right top) edge coordinates and axial slices (slices not to scale). (Right bottom) mesh detail.

The procedure used to extract the edge coordinates from the solid model included four steps. First, using the best fit cylinder to the tool shank and the fluted end's extreme point, the origin was established on the tool's center line. Second, the points located on the end mill's cutting edges were selected. This step required manual manipulation within the GOM software.

Third, the radius, r, and angle, ϕ, for each edge point was calculated in the local coordinate system. The teeth angles were normalized to a selected tooth and constrained to values between 0 and 360 deg; the z value was retained to obtain a triplet, $\{r, \phi, z\}$ for each point. Fourth, because the point density was higher than required for the time domain simulation, linear interpolation was used to obtain the triplet for axial slices located every 0.1 mm over the full cutting length; see Fig. 1, which displays the solid model and edge points for the focus tool of this study (Walter Tools, part number 3D1163-6768616).

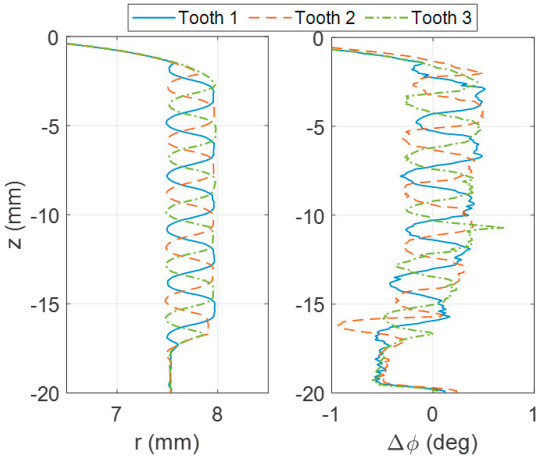

Fig. 2. Radius value (left) and deviations of teeth angles from nominal helix (right) at each axial slice for all three endmill teeth.

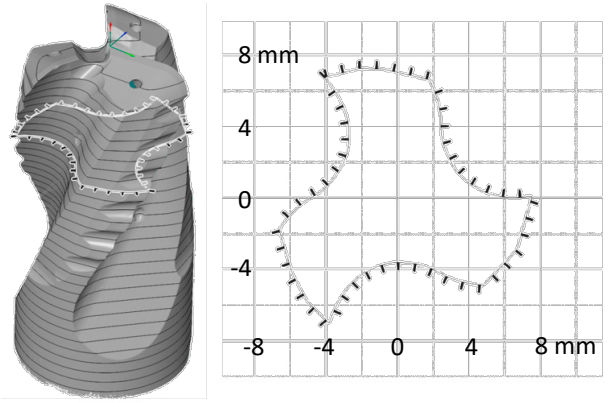

Fig. 3. (Left) Planar cross-sections of 3D model. (Right) z = -10 mm section showing rake and relief faces for all three teeth (right).

Example radius and angle results are provided in Fig. 2. It is observed in the left panel of Fig. 2 that the specialized tool geometry incorporates large radius variation along the cutting edge and that these radius variations are phased from one tooth to the next (120 deg spacing between the peaks for the three teeth). In the right panel of Fig. 2, it is seen that the angle variation from the nominal helix, $\Delta\phi$, is less than ±1 deg. Also, the point cloud data was used to determine the end mill's macro-geometry: 8 mm shank radius, 28.3 deg helix, and 2.785 mm bull nose radius.

4. Scanning metrology for rake and relief profiles

Similar to the Section 3 analysis, a coordinate system was established by fitting a cylinder to the tool shank and defining a plane at the fluted end's extreme point. The intersection of the cylinder's axis and the plane was set as the origin of the coordinate system. Planar cross-sections were then created along the tool's axis (z direction). Each section contained the rake and relief profiles of each tooth at the corresponding axial location; an example section is displayed in Fig. 3.

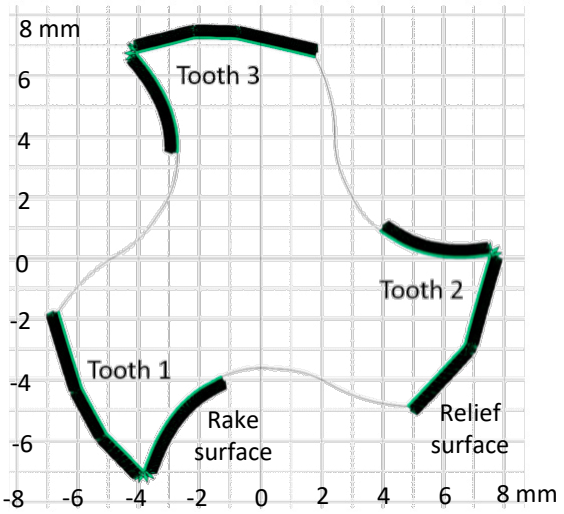

Fig. 4. Rake and relief points on each tooth for the z = -10 mm section.

To calculate the spatially-dependent rake and relief angles, equidistant points were placed along the rake and relief profiles; see Fig. 4, where the spacing between each point is 0.025 mm. Each point had an $\{x, y, z\}$ coordinate and unit normal vector. A reference vector was created by connecting the origin of the section to the center of the best-fit circle at the tooth tip, where the rake and relief profiles meet (Fig. 5). To measure the rake angles, the unit normal vectors along the rake profile were rotated 90 deg clockwise to become unit tangent vectors. The rake angle was the angle between the tangent vector and reference vector.

The same method was used to calculate the relief angles except the reference vector was now perpendicular (rotated 90 deg) to the original. The rake and relief angles were plotted with respect to point distance, which is the distance traversed along the rake or relief profile from tip to point. A point at the tip was selected as the zero point so the distance of each subsequent point, moving away from the tip, could be calculated based on the equidistant point spacing.

The rake and relief plots for tooth 1 are shown in Fig. 6. The rake angle is positive at the tip but flattens out and becomes negative as it moves further along the rake profile. The relief angle plot shows three angles corresponding to the three flat sections along the relief profile.

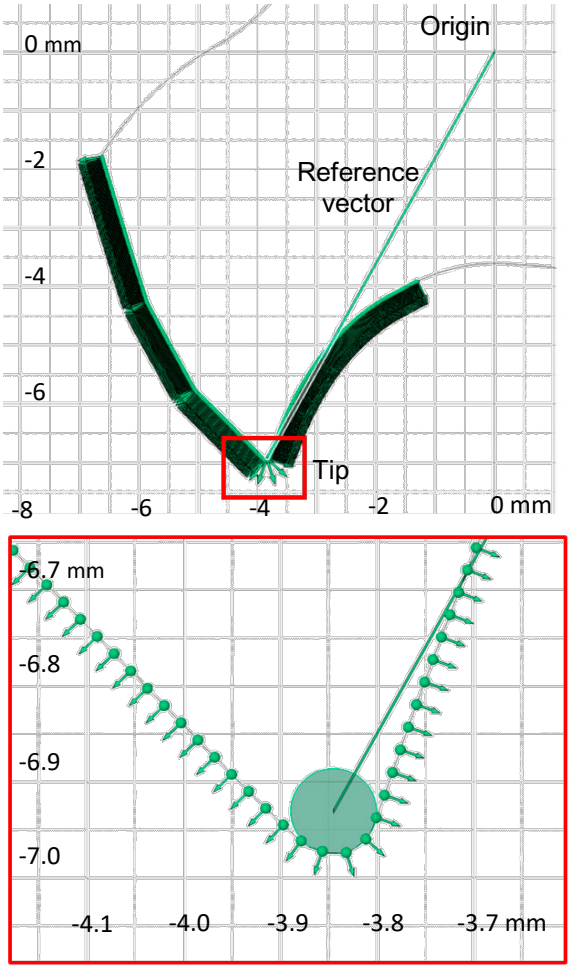

Fig. 5. (Top) reference vector. (Bottom) tip details of tooth 1 for the z = -10 mm section.

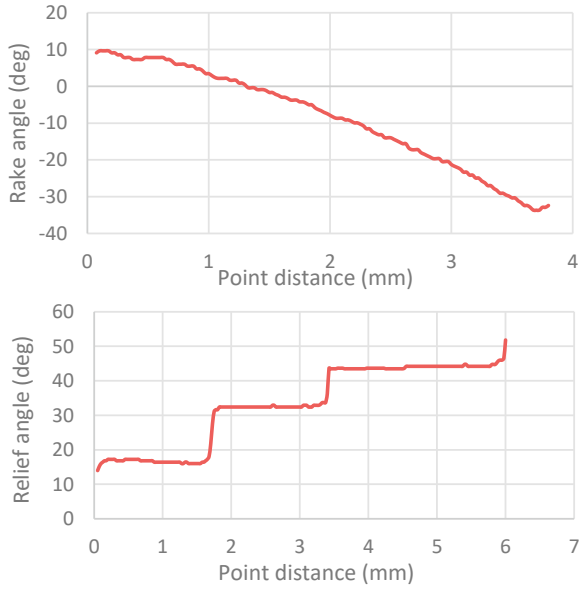

Fig. 6. Tooth 1 rake angle measurements for the z = -10 mm section (top). Tooth 1 relief angle measurements for the z = -10 mm section (bottom).

5. Time domain simulation description

Time domain simulation enables numerical solution of the coupled, time delay equations of motion for milling in small time steps [1]. It is well suited to incorporating the inherent complexities of milling dynamics, including complicated tool geometries (runout of the cutter teeth, non-uniform teeth spacing, and variable helix) and the nonlinearity that occurs if the tooth leaves the cut due to large magnitude vibrations. The simulation applied here is based on the regenerative force, dynamic deflection model described by Smith and Tlusty [19]. As opposed to analytical or semi-analytical stability maps that provide a global picture of the stability behavior, time domain simulation provides information regarding the local cutting force and vibration behavior for the selected cutting conditions. The simulation used in this study is described in the following paragraphs; it was previously validated for serrated cutter geometries [17-18].

The time domain simulation directly incorporated the measured tooth angles and radius variation displayed in Figs. 2 and 3. For the tooth angles, the measured angles from the scanned edge were arranged in an array, where the columns were the individual teeth and the rows were the z locations (in steps of 0.1 mm). A row array of closely spaced tooth angles for use in the time domain simulation was then defined. The resolution in this array was: $\Delta\phi = 360/SR$, where SR is the number of steps per revolution in the simulation.

Once this array was defined, the measured tooth angles were specified in an index array with each entry given by the ratio $\phi/\Delta\phi$ rounded to the nearest integer, where ϕ is the measured angle of the tooth at the selected z location. This index array was then used to specify the angle of any tooth at any z location by identifying the nearest preselected value from the closely spaced tooth angle array for use in the simulation. The reason for this approach is that the current chip thickness in milling depends not only on the commanded chip thickness and current vibration, but also the surface left by the previous teeth at the current tooth angle. To be able to do so conveniently, this information was organized according to specified tooth angles.

The radius variation for each tooth was included as runout, RO. The z-dependent RO values for each of the three teeth were also arranged in an array, where the columns were the individual teeth and the rows were the z locations (again in steps of 0.1 mm). All RO values were normalized to the maximum radius from all three teeth, which yielded negative RO values. A negative RO value reduces the chip thickness for the current tooth, but leaves behind material that the next tooth must remove (and therefore increases that chip thickness).

Two other data organization requirements were: 1) the surface that was left behind by the current tooth; and 2) the commanded chip thickness. To keep track of the previously machined surface, another array was defined that recorded the surface location in the tool's normal direction for each simulation time step. The columns of this matrix were the number of steps per revolution and the rows were the z locations. The influence of runout on subsequent chip thickness values was captured in this matrix. Because there were variations in the tooth angles from one tooth to the next, the commanded chip thickness was also modified to account for

the actual tooth angle using the circular tooth path approximation. This approximation calculates the nominal chip thickness from the product of the feed per tooth and the sine of the tooth angle.

Given this information, the simulation proceeded as follows:

1. The instantaneous chip thickness, $h(t)$, was determined using the commanded chip thickness, runout, and vibration of the current and previous teeth at the selected tooth angle.
2. The cutting force components in the tangential, t, and normal, n, directions were calculated at each axial slice using a mechanistic approach:

$$F_t(t) = k_t b h(t) \quad (1) \qquad F_n(t) = k_n b h(t) \quad (2)$$

where b is the slice width (0.1 mm) and the cutting force coefficients are identified by the subscripts t or n for direction. These forces were then summed over all axial slices engaged in the cut.

3. The summed force components were used to find the new displacements by numerical solution of the differential equations of motion in the x (feed) and y directions:

$$m_x\ddot{x} + c_x\dot{x} + k_x x = F_t(t)\cos\phi + F_n(t)\sin\phi \quad (3)$$

$$m_y\ddot{y} + c_y\dot{y} + k_y y = F_t(t)\sin\phi - F_n(t)\cos\phi \quad (4)$$

where m is the modal mass, c is the modal viscous damping coefficient, and k is the modal stiffness. The subscripts identify the direction and multiple degrees-of-freedom in each direction can be accommodated by summing the modal contributions [1-2].

4. The tool rotation angle was incremented by adding one to each entry in the tooth angle index array and the process was repeated.

A flowchart is provided in Fig. 7 to summarize the simulation steps.

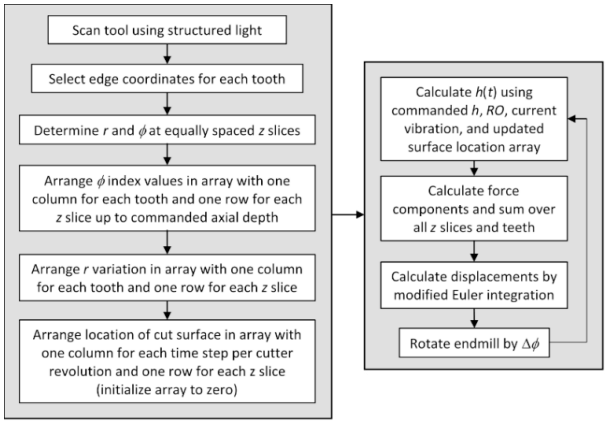

Fig. 7. Time domain simulation flowchart. (Left) setup information. (Right) simulation steps.

6. Force modeling

There are two options for determining the cutting force coefficients, k_t and k_n, in Eqs. 1 and 2. First, cutting tests may be completed where the axial depth, radial depth, and feed per tooth values are prescribed, the force components are measured for the desired tool-work material pair using a cutting force dynamometer, and a least-squares best fit is used to calculate the force coefficients [1-2, 20]. Second, finite element simulation may be applied to predict the cutting force components using the work material's constitutive relationship (e.g., the Johnson-Cook model [21]) and machining parameters. The latter was selected for this digital study, where orthogonal cutting simulations were completed using AdvantEdge™ from Third Wave Systems [22].

To calculate the cutting force coefficients, the following procedure was followed:

1. The archived 7075-T6 material model was selected. The tool material was set as carbide.
2. The cutting edge cross-sectional geometry was imported as a series of points that defined the rake and relief surface profiles (see Fig. 5).
3. The orthogonal cutting parameters were specified including the cutting speed, chip width, and chip thickness. For milling, the cutting speed defines the spindle speed given the end mill radius, the chip width is the 0.1 mm slice width in the modeling scheme, and the instantanous chip thickness is set by the commanded feed per tooth and tooth angle as the rotating end mill proceeds through the cut.
4. The simulation was completed and the mean feed direction, F_t, and surface normal direction, F_n, force values were recorded (initial transients at cut entry and final transients at cut exit were excluded).
5. The force coefficients were calculated by dividing the force components by the uncut chip area (i.e., the product of the chip width and thickness as shown in Eqs. 1 and 2).
6. The chip thickness was modified and steps 4 and 5 were repeated.

The final step was included due to the dramatic change in rake angle near the cutting edge radius. At this tip location (Fig. 6), the local rake angle transitions from positive to highly negative at the chip thickness is decreased. Figure 8 displays the variation in the cutting force coefficients with chip thickness.

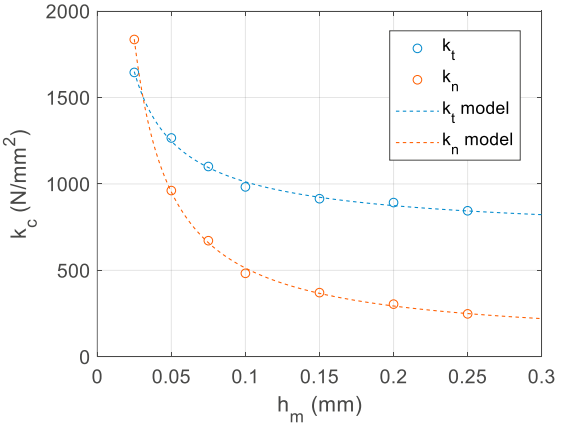

Fig. 8. Cutting force coefficient values (circles) for 6061-T6 work material and measured rake/relief geometry for carbide end mill predicted by finite element analysis. The results are presented as a function of commanded (or mean) chip thickness, h_m. The data points were fit to obtain the k_t and k_n models (dashed lines).

These points were fit in a least-squares sense to define the final cutting force coefficient functions provided in Eqs. 5 and 6. Within the time domain simulation, the actual coefficient values were determined in each time step using the instantaneous chip thickness to evaluate the functions in Eqs. 5 and 6.

$$k_t = 56.17 {h_m}^{-0.7723} + 679.9 \text{ N/mm}^2 \quad (5)$$

$$k_n = 43.40 {h_m}^{-1.005} + 75.68 \text{ N/mm}^2 \quad (6)$$

7. Cutting force comparison

The experimental setup for milling force measurement is shown in Fig. 9. Trials were completed on a Haas TM-1 three-axis computer numerically controlled (CNC) milling machine. The 7075-T6 aluminum workpiece was mounted on a cutting force dynamometer (Kistler 9257B) and the endmill was clamped in a collet holder and inserted in the CAT-40 spindle interface. Tests were performed at axial depths of cut from 4 mm to 14 mm. The commanded feed per tooth for these down (climb) milling experiments was 75 µm/tooth, the spindle speed was 4000 rpm, and the radial depth of cut was 2 mm (12.5% radial immersion).

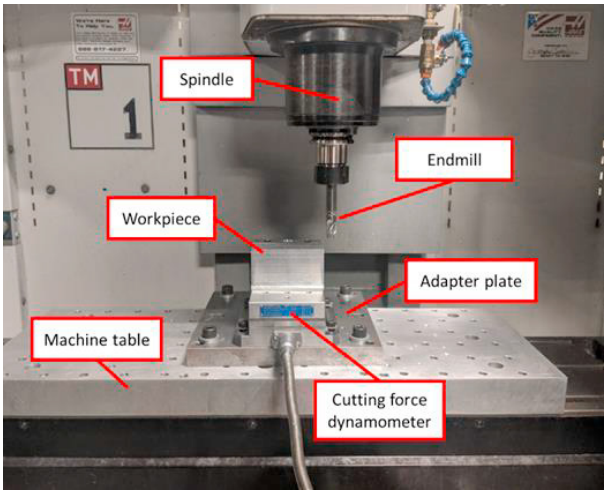

Fig 9. Experimental setup for milling force measurement.

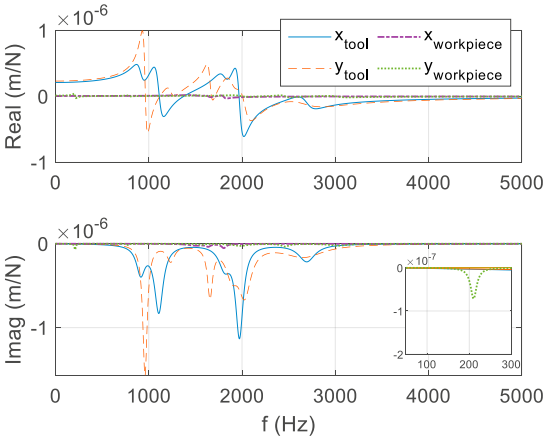

Fig. 10. Measured FRFs for tool and workpiece.

The tool and workpiece frequency response functions, or FRFs, were measured by impact testing, where an instrumented hammer is used to excite the structure and the response is measured using a linear transducer (a low-mass accelerometer for this research). The results are displayed in Fig. 10. Modal fitting was applied to extract the modal parameters for the time domain simulation; see Appendix B.

The same spindle speed and radial depth were used. Measured and predicted force values, F_x (feed direction) and F_y, for b = {4, 6, 8, 12, and 14} mm are shown in Figs. 11-15. Good agreement is observed in all cases, where the dynamometer results were inverse filtered to remove the influence of the dynamometer dynamics; see Appendix C. It is seen that the force progresses from a smooth profile while engaged in the cut for b = 4 mm to highly discontinuous at b = 14 mm. This is the result of the tool design which cuts with "bands" of limited axial depth, where this depth is defined by the spatial period of the radius variation along the tooth helix (Fig. 2). As the axial depth increases, more bands are individually engaged and the force is subsequently increasingly discontinuous.

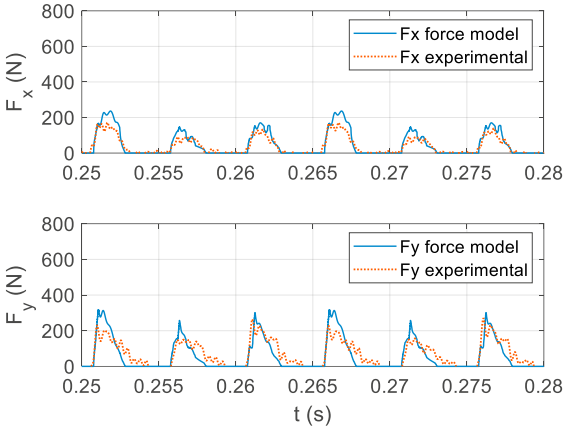

Fig. 11. Cutting forces for 4 mm axial depth.

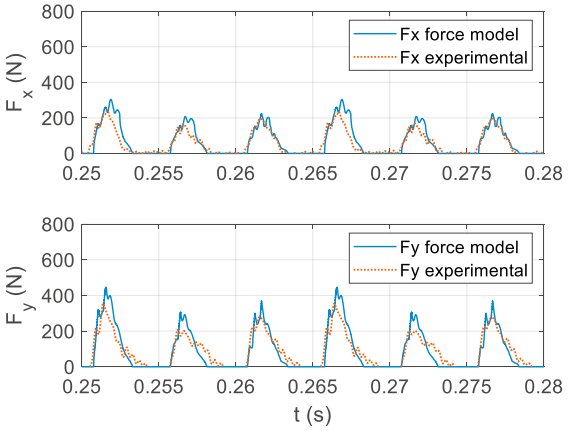

Fig. 12. Cutting forces for 6 mm axial depth.

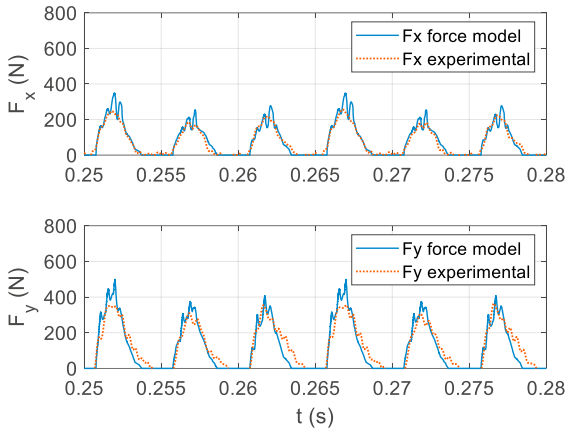

Fig. 13. Cutting forces for 8 mm axial depth.

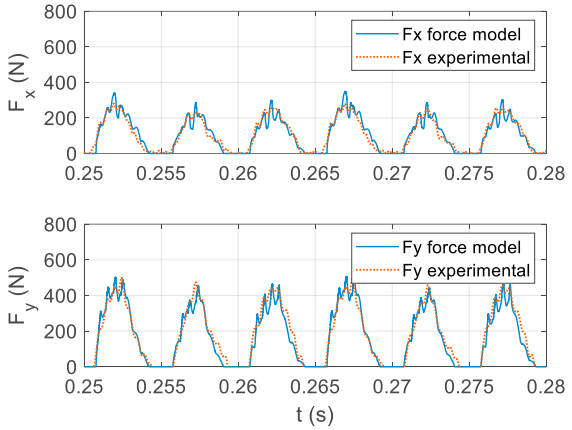

Fig. 14. Cutting forces for 12 mm axial depth.

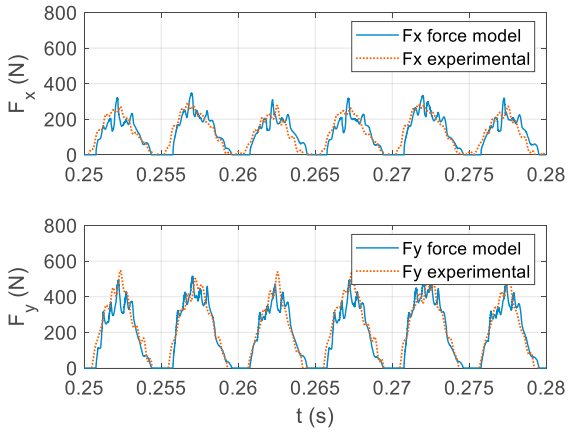

Fig. 15. Cutting forces for 14 mm axial depth.

In a second set of tests, the axial depth was held constant at 8 mm and the feed per tooth was varied from 25 µm/tooth to 125 µm/tooth. Figures 16-20 display measured and predicted F_x and F_y results for feed per tooth values of {25, 50, 75, 100, and 125} µm/tooth. While the force levels grow with the increased chip thickness, they do not become considerably more discontinuous. This is because the axial depth was fixed at 8 mm for these tests.

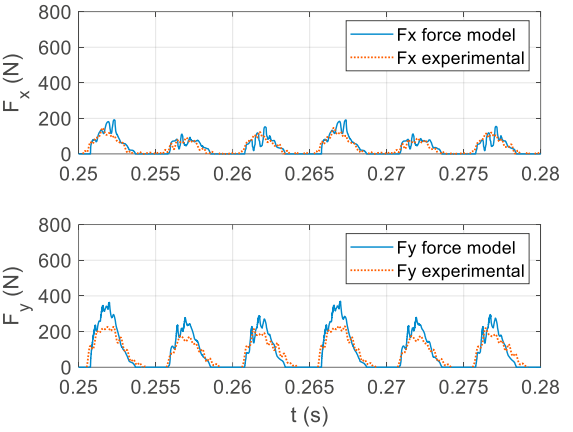

Fig. 16. Measured and predicted forces for f_t = 25 µm/tooth.

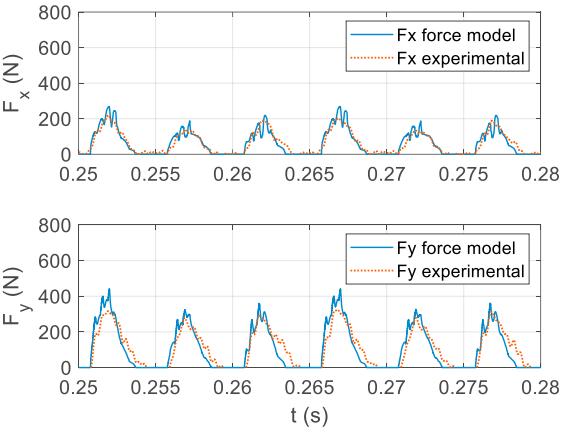

Fig. 17. Measured and predicted forces for f_t = 50 µm/tooth.

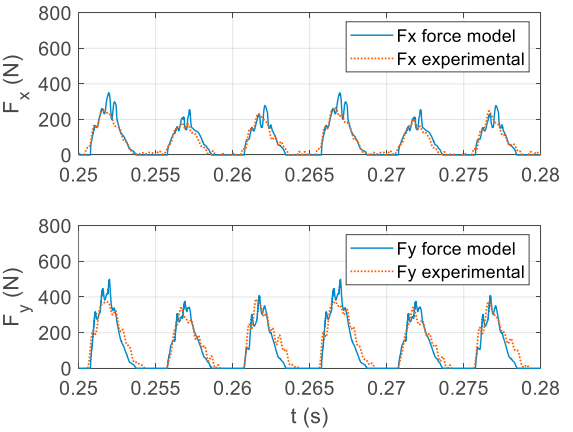

Fig. 18. Measured and predicted forces for f_t = 75 µm/tooth.

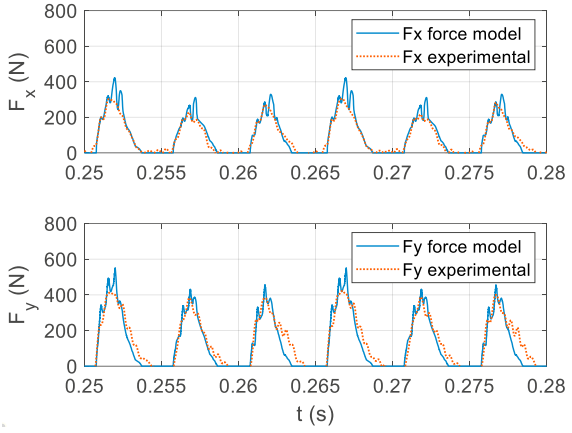

Fig. 19. Measured and predicted forces for f_t = 100 μm/tooth.

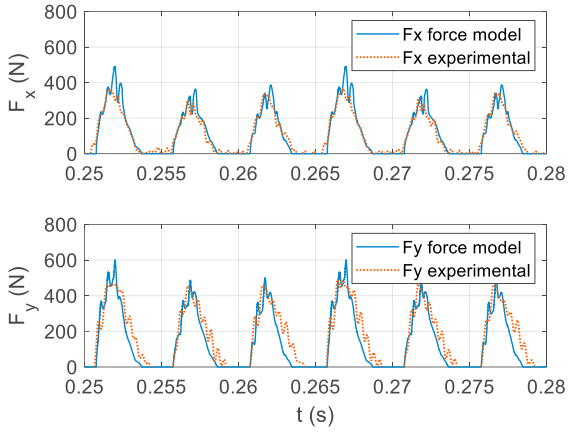

Fig. 20. Measured and predicted forces for f_t = 125 μm/tooth.

8. Conclusions

This paper provided a fully digital solution for modeling cutting force in milling. Structured light scanning was used to produce a solid model of an example end mill. From this model, spatial coordinates for the points that define the insert cutting edges were extracted. The points were used to determine the cutting edge radius and angle at equally spaced points along the tool's axis. Additionally, the rake and relief profiles for the tool's cross-section were measured and used in finite element analysis to predict the force components for orthogonal cutting. The chip thickness-dependent cutting force coefficients were calculated and nonlinear functions were fit to the data points. The digital cutting edge geometry and force model were then incorporated in a time domain simulation that was used to predict cutting force for user-selected operating parameters. Good agreement between predicted and measured cutting forces was obtained.

Acknowledgements

The authors gratefully acknowledge financial support from the National Science Foundation (CMMI-1561221). Additionally, this research was supported by the DOE Office of Energy Efficiency and Renewable Energy (EERE), Energy and Transportation Science Division and used resources at the Manufacturing Demonstration Facility, a DOE-EERE User Facility at Oak Ridge National Laboratory. Finally, the authors gratefully fully acknowledge support from Third Wave Systems for the use of AdvantEdge™ in this study.

References

[1] Schmitz, T.L. and Smith, K.S., 2019. Machining Dynamics: Frequency Response to Improved Productivity, 2nd Ed., Springer, New York.
[2] Altintas, Y., 2012. Manufacturing Automation: Metal Cutting Mechanics, Machine Tool Vibrations, and CNC Design, Cambridge University Press.
[3] Altintas, Y. and Weck, M., 2004. Chatter stability of metal cutting and grinding. CIRP Annals-Manufacturing Technology, 53(2), pp.619-642.
[4] Fu, H.J., DeVor, R.E. and Kapoor, S.G., 1984. A mechanistic model for the prediction of the force system in face milling operations. Journal of engineering for industry, 106(1), pp.81-88.
[5] Kim, H.S. and Ehmann, K.F., 1993. A cutting force model for face milling operations. International Journal of Machine Tools and Manufacture, 33(5), pp.651-673.
[6] Zheng, H.Q., Li, X.P., Wong, Y.S. and Nee, A.Y.C., 1999. Theoretical modelling and simulation of cutting forces in face milling with cutter runout. International Journal of Machine Tools and Manufacture, 39(12), pp.2003-2018.
[7] Engin, S. and Altintas, Y., 2001. Mechanics and dynamics of general milling cutters: Part II: Inserted cutters. International Journal of Machine Tools and Manufacture, 41(15), pp.2213-2231.
[8] Altintas, Y. and Engin, S., 2001. Generalized modeling of mechanics and dynamics of milling cutters. CIRP Annals, 50(1), pp.25-30.
[9] Wang, J.J.J. and Yang, C.S., 2003. Angle and frequency domain force models for a roughing end mill with a sinusoidal edge profile. International Journal of Machine Tools and Manufacture, 43(14), pp.1509-1520.
[10] Merdol, S.D. and Altintas, Y., 2004. Mechanics and dynamics of serrated cylindrical and tapered end mills. Journal of Manufacturing Science and Engineering, 126(2), pp.317-326.
[11] Dombovari, Z., Altintas, Y. and Stepan, G., 2010. The effect of serration on mechanics and stability of milling cutters. International Journal of Machine Tools and Manufacture, 50(6), pp.511-520.
[12] Dombovari, Z., Munoa, J. and Stepan, G., 2012. General milling stability model for cylindrical tools. Procedia CIRP, 4, pp.90-97.
[13] Stépán, G., Munoa, J., Insperger, T., Surico, M., Bachrathy, D. and Dombóvári, Z., 2014. Cylindrical milling tools: comparative real case study for process stability. CIRP Annals, 63(1), pp.385-388.
[14] Koca, R. and Budak, E., 2013. Optimization of serrated end mills for reduced cutting energy and higher stability. Procedia CIRP, 8, pp.570-575.
[15] Grabowski, R., Denkena, B. and Köhler, J., 2014. Prediction of process forces and stability of end mills with complex geometries. Procedia CIRP, 14, pp.119-124.
[16] Tehranizadeh, F. and Budak, E., 2017. Design of serrated end mills for improved productivity. Procedia CIRP, 58, pp.493-498.
[17] No, T., Gomez, M., Copenhaver, R., Perez, J.U., Tyler, C. and Schmitz, T.L., 2019. Force and stability modeling for non-standard edge geometry endmills. Journal of Manufacturing Science and Engineering, 141(12).
[18] No, T., Gomez, M., Copenhaver, R., Perez, J.U., Tyler, C. and Schmitz, T.L., 2019. Scanning and modeling for non-standard edge geometry endmills. Procedia Manufacturing, 34, pp.305-315.
[19] Smith, K.S. and Tlusty, J., 1991. An overview of modeling and simulation of the milling process. ASME Journal of Engineering for Industry, 113(2), pp.169-175.
[20] Rubeo, M. and Schmitz, T., 2016. Milling force modeling: A comparison of two approaches. Procedia Manufacturing, 5, pp.90-105.
[21] Johnson G. R. and Cook W. H., 1983. A constitutive model and data for metals subjected to large strains, high strain rates and high temperatures. In: 7th International Symposium on Ballistics, pp.514-546.
[22] https://www.thirdwavesys.com/advantedge/.

Appendix A. Structured light scanning setup

A GOM ATOS Capsule was used to measure the end mill geometry; see Fig. A1.

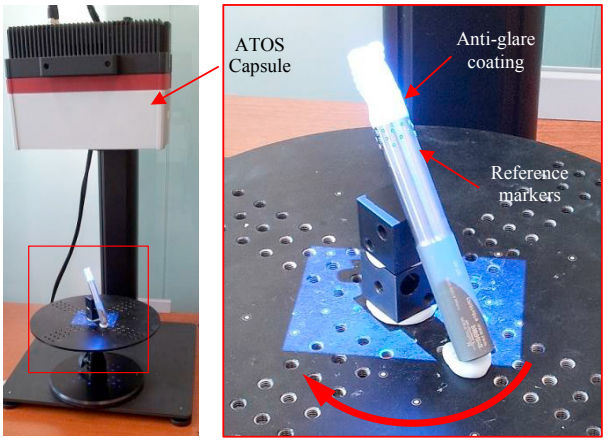

Fig. A1. Structured light scanning setup.

Appendix B. Modal parameters

The modal parameters obtained from fitting the measured FRFs for the tool and workpiece are provided in Table B1.

Table B1. Modal parameters for force measurement setup.

Tool			
Direction	m (kg)	k (N/m)	c (N-s/m)
x	0.756	2.50×10^{7}	522
x	0.257	1.25×10^{7}	179
x	0.381	4.95×10^{7}	348
x	0.120	1.85×10^{7}	75
x	0.209	6.00×10^{7}	283
y	0.294	1.07×10^{7}	105
y	1.101	6.65×10^{7}	106
y	0.392	4.25×10^{7}	684
y	27.774	4.00×10^{7}	162
y	0.140	2.27×10^{7}	2666
y	0.118	3.33×10^{7}	142
Workpiece			
Direction	m (kg)	k (N/m)	c (N-s/m)
x	0.373	3.37×10^{7}	496
x	1.039	1.10×10^{8}	363
x	0.466	6.00×10^{7}	180
x	0.019	1.12×10^{7}	232
y	95.576	1.67×10^{8}	10612
y	73.651	1.77×10^{9}	12276
y	21.054	2.03×10^{9}	7856
y	2.780	4.32×10^{8}	3258
y	3.203	7.67×10^{8}	1983
y	1.616	5.87×10^{8}	2279

Appendix C. Dynamometer inverse filtering

To remove the effects of the dynamometer's structural dynamics on the measured force, the dynamometer force-to-force FRFs were measured by impact testing. The x, y, and z direction FRFs are displayed in Fig. C1. These FRFs were inverted and low pass filtered (third-order Butterworth with 2000 Hz cutoff frequency) and subsequently used to filter the measured cutting forces. The inverse filters are displayed in Fig. C2.

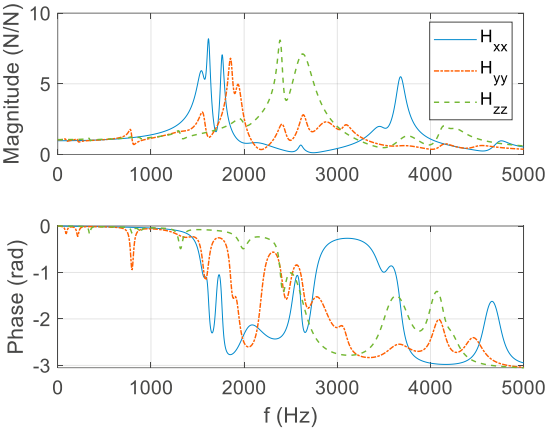

Fig. C1. Measured dynamometer FRFs.

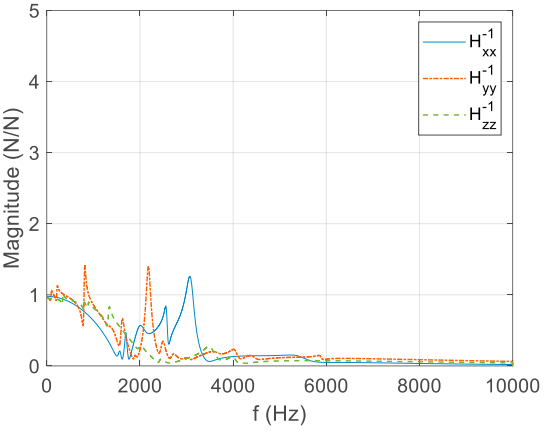

Fig. C2. Inverse filters used to correct the effects of the dynamometer dynamics on the measured forces.